scientific reports

OPEN

Mapping neutron biological effectiveness for DNA damage induction as a function of incident energy and depth in a human sized phantom

Alice Mentana[1], Virgilio Quaresima[1], Pavel Kundrát[2], Isabella Guardamagna[1], Leonardo Lonati[1], Ombretta Iaria[1], Andrea Previtali[1], Giorgia Santi Amantini[3], Luca Lunati[3], Virginia Boretti[3], Livio Narici[3], Luca Di Fino[4], Luca Bocchini[5], Claudio Cipriani[5] & Giorgio Baiocco[1]✉

We present new developments for an ab-initio model of the neutron relative biological effectiveness (RBE) in inducing specific classes of DNA damage. RBE is evaluated as a function of the incident neutron energy and of the depth inside a human-sized reference spherical phantom. The adopted mechanistic approach traces neutron RBE back to its origin, i.e. neutron physical interactions with biological tissues. To this aim, we combined the simulation of radiation transport through biological matter, performed with the Monte Carlo code PHITS, and the prediction of DNA damage using analytical formulas, which ground on a large database of biophysical radiation track structure simulations performed with the code PARTRAC. In particular, two classes of DNA damage were considered: sites and clusters of double-strand breaks (DSBs), which are known to be correlated with cell fate following radiation exposure. Within a coherent modelling framework, this approach tackles the variation of neutron RBE in a wide energy range, from thermal neutrons to neutrons of hundreds of GeV, and reproduces effects related to depth in the human-sized receptor, as well as to the receptor size itself. Besides providing a better mechanistic understanding of neutron biological effectiveness, the new model can support better-informed decisions for radiation protection: indeed, current neutron weighting (ICRP)/quality (U.S. NRC) factors might be insufficient for use in some radiation protection applications, because they do not account for depth. RBE predictions obtained with the reported model were successfully compared to the currently adopted radiation protection standards when the depth information is not relevant (at the shallowest depth in the phantom or for very high energy neutrons). However, our results demonstrate that great care is needed when applying weighting factors as a function of incident neutron energy only, not explicitly considering RBE variation in the target. Finally, to facilitate the use of our results, we propose look-up RBE tables, explicitly considering the depth variable, and an analytical representation of the maximal RBE vs. neutron energy.

Neutrons are indirectly ionizing radiation, since they carry no charge and therefore cannot interact with atomic electrons in matter via Coulomb force, which is the dominant energy loss process for charged particles. For this reason, e.g. a neutron in the MeV energy range may travel through biological matter several centimeters without any energy loss or change in direction. Neutron interactions occur with atomic nuclei of the target material: as a result, the neutron can be totally absorbed, with the emission of secondary radiation, or significantly change its energy or direction[1]. The mixed radiation field generated by neutron interactions consists of photons and charged particles, produced via neutron-induced nuclear reactions, and target recoiling nuclei that gain energy via neutron collisions. The relative probability (cross-section) of a specific nuclear reaction, thus of the production of a specific secondary radiation, is strongly dependent on the neutron incoming energy. This deserves special

[1]Radiation Biophysics and Radiobiology Laboratory, Physics Department, University of Pavia, Pavia, Italy. [2]Department of Radiation Dosimetry, Nuclear Physics Institute, Czech Academy of Sciences, Prague, Czechia. [3]Physics Department, University of Roma Tor Vergata, Rome, Italy. [4]ASI, Italian Space Agency, Rome, Italy. [5]Thales Alenia Space-Italy, Turin, Italy. ✉email: giorgio.baiocco@unipv.it

attention, in particular for its biological implications: the amount of energy deposited by radiation is generally quantified in terms of physical absorbed dose, i.e. energy deposited per unit mass. However, it is well known that equal doses of different radiation qualities produce different biological effects, and this is mainly due to the different energy deposition pattern at the microscopic/nanoscopic scale[2].

The relative biological effectiveness (RBE) is a quantity introduced in radiation biology to compare biological effects of different radiation qualities. It is defined as the ratio between the doses of a reference and a test radiation needed to produce the same biological effects. Low-LET radiation, in particular from ^{60}Co γ-rays or 250 kVp X-rays, is generally chosen as the reference. From its definition it is clear that the RBE of a test radiation depends (among other factors) on the biological effect (endpoint) considered. Experimental RBE measurements provide information for the definition of the so-called radiation weighting factors w_R, which are used in radiation protection to convert physical absorbed dose into equivalent dose, thus accounting for the differences in biological effectiveness of different radiation qualities. Radiation weighting factors have been established and are constantly being revised by the International Commission for Radiation Protection (ICRP). Their values are agreed upon by the Commission and the radiation protection community to be representative of the maximal RBE of the test radiation in inducing stochastic effects at low-doses[3,4]. As explicitly stated by the ICRP, w_R should be intended only for radiation protection purposes but not for risk assessment, since, for the sake of simplicity, they are provided irrespective of endpoint, dose rate, tissue etc. Ideally, the determination of w_R values would be predominantly based on RBE data from in-vivo investigations related to stochastic effects. In-vitro studies with cells provide important mechanistic understanding, but RBE values obtained in these studies might not be clearly correlated with carcinogenesis in humans. However, only limited data are available from animal studies (and from epidemiological studies) in the range of radiation qualities of interest. The strategy to establish weighting factors is therefore based on obtaining a quality factor dependence on LET (Q(L)), mainly based on in-vitro experiments, then used to calculate a mean Q value for the human body, which in turn is used to estimate weighting factors. This is especially the case for protons, heavy ions, and, to some extent, for neutrons[4].

In light of the above discussion, it is clear that neutron RBE, and therefore radiation weighting factors w_R, depend on neutron energy. This is a direct consequence of the strong dependence of the secondary mixed radiation field, generated by neutron interactions through matter, on neutron incoming energy. This aspect, together with the examination and inclusion of new available experimental data, represents the reason why the adopted radiation protection standards for neutrons undergo steady reviewing. As a relevant example, neutron w_R's have been re-evaluated from ICRP Publication 60, published in 1991,[3] to ICRP Publication 92 in 2003[5]: the original values were obtained translating the results from in-vivo mice experiments to humans without properly taking into account the increased photon component of the neutron dose, when low-energy neutrons interact in a larger size receptor. Indeed, particular attention should be paid to the target dimensions: large target sizes might result in neutron moderation, which in turns implies a change in energy and hence in biological effectiveness. In ICRP Publication 92 the previously given discontinuous function of neutron energy was also substituted with a continuous analytical parameterization of w_R: this better reflects the characteristics of experimental setups used to obtain radiobiological data, as neutron sources are never strictly monoenergetic, and becomes more practical for radiation protection implementations, as folding of energy distributions with w_R functions might be needed. Going from ICRP Publication 92 to ICRP Publication 103[4], w_R values for neutrons above 1 GeV have also been further reduced and set to an asymptotic value, based on theoretical expectations, as experimental radiobiological data for neutrons of such high energies are basically impossible to obtain.

When comparing ICRP neutron weighting factors to the analogous U.S. NRC neutron quality factors[6], adopted in the US radiation protection system, it is clearly noticeable how radiation protection standards are also dependent on the experimental data-set selected for their evaluation[7]. While the two standards agree on biological effectiveness of neutrons being maximal at energies around 1 MeV, the corresponding absolute values of weighting and quality factors differ by a factor of two. Furthermore, in the U.S. NRC standard, a second peak of effectiveness for neutrons around 20 MeV is considered, which is absent in the ICRP data. Finally, and most importantly for the application of results presented in this work, current radiation protection standards for neutrons do not explicitly take into account the depth in the exposed human subject, as weighting or quality factors are established as a function of incident neutron energy only. As such, they might be insufficient for use in many relevant radiation protection scenarios, as the possible RBE variation in the target is not properly taken into account.

In this framework, theoretical approaches aiming at tracing back neutron biological effectiveness to primary neutron interactions can be of great help. Thus far, few neutron RBE models exist in the literature, some related to neutron therapy applications[8,9], up to a recent RBE model for the DNA damage induction[10]. A first model based on a fully mechanistic approach was proposed by Baiocco et al.[11], to determine the energy dependence of neutron RBE for DNA damage, specifically considering as damage endpoint clusters of double-strand breaks (at least 2 DSBs within a genomic lenght of 25 bp). In recent works[12,13], a similar approach has been used to model the neutron RBE for the induction of DNA damage, showing a substantial agreement in the RBE energy dependence, though generally lower RBE values with respect to those found in Baiocco et al.[11].

The work presented here follows and updates the modelling strategy proposed in Baiocco et al.[11], coupling the capabilities of different simulation approaches: the Monte Carlo transport code PHITS[14] has been used characterize neutron interactions inside a biological target of a human size. The characterization of energy deposition by secondary species in the neutron-induced mixed field has been conducted at the sub-cellular level with a microdosimetry approach. Such information has then been used to predict the DNA damage as a function of neutron energy, using analytical functions that capture how yields of DSB sites and clusters depend on the linear energy transfer at the cell nucleus scale[15]. These functions were derived from a large database of Monte Carlo track-structure simulation results obtained with the code PARTRAC[16–18]. Neutron RBE values for the induction of different classes of DNA damage have finally been evaluated, comparing predicted neutron effects to those due to a reference radiation.

With respect to the previous model, the spatial variation of neutron RBE has now been fully mapped in a large-sized receptor, allowing in perspective for the correlation between predicted DNA damage endpoints and associated biological consequences at different depths (hence, organs) in an exposed subject. The neutron energy range for RBE evaluation has also been extended, both below the thermal energy of ≈ 25 meV and in the high energy region, up to 100 GeV. Refined and more accurate analytical formulas of DNA damage vs. linear energy transfer in the cell nucleus have been used. DSB sites have been included as a relevant class of DNA damage, as their simulated yields as a function of LET show the typical behaviour of the RBE for cell killing, with ion-specific peaks in the range 100–200 keV/µm, thus reproducing the so-called overkilling effect. DSB clusters are still considered: the relevance of clustered DNA damage is well recognised within the radiation biology community[19–21], and the induction of this kind of damage also leads to the maximal RBE, which is of interest for radiation protection applications. Overall, these new developments widen the possible scenarios to obtain neutron RBE predictions, with a full mapping of the dependence on energy and depth in a human-sized receptor, also reproducing the dependence on the receptor size. To facilitate the use of our results, look-up tables of neutron RBE values, explicitly considering the depth variable, and an analytical representation of the maximal RBE vs. incident energy are finally proposed. This model can provide predictions to be benchmarked againts experimental radiobiological data, with the potential, in perspective, to inform RBE—risk correlations and the work of radiation protection commissions.

Methods

We adopted the strategy presented in Baiocco et al.[11], based on the coupling of radiation transport and track-structure simulations, with the introduction of refinements, specifically concerning the spatial mapping of neutron-induced DNA damage yields and RBE in the full geometry of the human-sized receptor, and the use of new analytical functions to predict DNA damage.

Neutron transport calculations with PHITS in a human-sized phantom

Simulations were performed using the Monte Carlo radiation transport code PHITS (Particle and Heavy Ion Transport code System, v. 3.22)[14], able to deal with the transport of all particles over wide energy ranges, using several reaction models and data libraries[22,23]. The so-called Event Generator Mode[24], calculating event-by-event quantities using cross-sections from the evaluated nuclear data library JENDL-4.0, was used for neutron incident energies below 20 MeV. For higher neutron energies, JAM and JAMQMD models are implemented to simulate particle-induced reactions up to 3 GeV and nucleus-nucleus collisions, respectively.

We simulated the exposure of an ICRU sphere to monoenergetic and isotropic neutron sources (see panel (a) of Fig. 1) in the energy range 10^{-8}–10^{5} MeV. All neutron energy values E_n are listed explicitly in Table 1. Neutrons are emitted using the isotropic source option available in the PHITS source input (*dir* = *iso*), directly at the phantom external surface. The ICRU sphere is a simple but commonly adopted reference phantom, made of ICRU44 soft tissue[25] and with radius R = 15 cm, representative of the human trunk. In this work, the sphere has been further divided into 15 isocentric shells, 1 cm thick, considered as different scoring regions. The spherical shell geometry is chosen to take into account the depth in the phantom, considering the phantom symmetry and the isotropy of the radiation field. All quantities of interest have been calculated for each shell, thus obtaining a full set of results as a function of the depth. The thickness of the layer has been set to 1 cm, particularly to provide

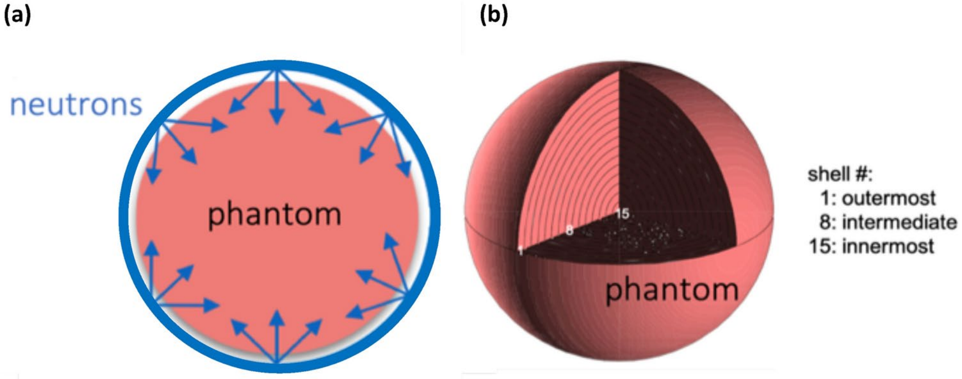

Fig. 1. Panel (**a**): illustration of the irradiation geometry of the ICRU sphere phantom (in pink), in an isotropic monoenergetic neutron field (blue circle as the neutron source surface, corresponding to the phantom external surface, and arrows as neutron directions). Panel (**b**): three-dimensional view of the spherical phantom software implementation in PHITS, with a cut-away section to show the inner structure with 15 isocentric shell regions. Representative regions referred to in the text as the outermost (#1, average depth: 0.5 cm), intermediate (#8, average depth: 7.5 cm) and innermost (#15, average depth: 14.5 cm) ones are also indicated in the Figure. The elemental composition of the ICRU-44 tissue is: H(10.2%) + C(14.3%) + N(3.4%) + O(70.8%) + Na(0.2%) + P(0.3%) + S(0.3%) + Cl(0.2%) + K(0.3%).

neutron RBE (DSB clusters)															
	shell ♯ [mean depth (cm)]														
E_n **(MeV)**	**1[0.5]**	**2[1.5]**	**3[2.5]**	**4[3.5]**	**5[4.5]**	**6[5.5]**	**7[6.5]**	**8[7.5]**	**9[8.5]**	**10[9.5]**	**11[10.5]**	**12[11.5]**	**13[12.5]**	**14[13.5]**	**15[14.5]**
10^{-8}	4.1	2.9	2.5	2.3	2.0	1.9	1.8	1.7	1.6	1.6	1.5	1.5	1.4	1.5	1.6
10^{-7}	3.4	3.0	2.6	2.4	2.2	2.0	1.9	1.8	1.7	1.6	1.5	1.5	1.4	1.4	1.3
10^{-6}	3.0	3.0	2.8	2.6	2.3	2.1	2.0	1.8	1.7	1.7	1.6	1.6	1.5	1.6	1.6
0.0001	2.4	2.8	2.8	2.7	2.5	2.3	2.2	2.0	1.9	1.8	1.7	1.7	1.6	1.6	1.5
0.001	2.0	2.6	2.7	2.7	2.5	2.4	2.2	2.1	2.0	1.9	1.8	1.7	1.7	1.6	1.9
0.01	2.3	2.3	2.5	2.6	2.5	2.4	2.3	2.2	2.1	2.0	1.9	1.8	1.8	1.8	1.7
0.1	10.0	6.7	4.6	3.5	2.9	2.6	2.4	2.3	2.1	2.1	2.0	1.9	1.9	1.8	1.8
0.2	14.5	11.0	8.3	6.0	4.5	3.5	2.9	2.6	2.4	2.2	2.2	2.0	1.9	1.9	2.2
0.5	16.1	14.7	13.1	11.3	9.4	7.8	6.4	5.3	4.5	3.8	3.5	3.0	2.7	2.7	2.8
0.8	14.2	13.8	13.2	12.2	11.2	10.1	8.9	7.8	7.1	6.3	5.7	5.3	4.9	4.6	3.9
1	13.8	13.6	13.1	12.3	11.4	10.3	9.2	8.3	7.3	6.7	5.9	5.5	5.0	4.8	4.3
2.5	7.6	8.0	8.2	8.3	8.4	8.5	8.4	8.4	8.3	8.1	8.2	8.0	8.1	7.9	8.0
5	6.0	6.2	6.3	6.4	6.5	6.6	6.6	6.6	6.7	6.6	6.7	6.6	6.5	6.6	6.7
7.5	5.6	5.6	5.7	5.7	5.7	5.8	5.8	5.8	5.8	5.8	5.8	5.9	5.7	5.7	5.7
10	7.1	7.0	6.9	6.8	6.8	6.8	6.6	6.6	6.6	6.8	6.5	6.5	6.5	6.3	6.4
15	8.7	8.4	8.3	8.1	8.1	8.0	8.1	7.8	7.9	7.8	7.8	7.7	7.5	7.8	7.9
17.5	10.3	10.0	9.9	9.6	9.5	9.4	9.4	9.2	9.1	9.1	9.2	9.1	9.0	9.0	8.8
20	11.0	10.4	10.4	10.2	10.1	10.1	10.0	10.1	9.6	9.8	9.7	9.7	9.7	9.7	11.0
22.5	8.9	8.5	8.5	8.4	8.4	8.3	8.3	8.3	8.2	8.2	8.2	8.2	8.2	8.3	8.2
25	8.4	8.2	8.1	7.9	8.1	7.9	7.9	8.1	8.0	7.9	7.8	7.7	7.4	7.6	8.2
50	6.6	5.9	6.0	6.0	6.0	6.1	6.0	5.9	6.0	5.9	5.9	6.2	6.0	6.2	5.4
100	5.2	4.6	4.4	4.3	4.3	4.3	4.3	4.3	4.4	4.2	4.3	4.2	4.2	4.5	4.9
500	3.9	3.5	3.4	3.3	3.2	3.1	3.1	3.1	3.0	3.0	3.0	3.0	3.0	3.0	3.1
1000	3.4	3.1	3.0	2.9	2.8	2.8	2.8	2.7	2.7	2.7	2.7	2.7	2.7	2.7	2.7
10000	2.6	2.5	2.4	2.4	2.3	2.3	2.3	2.3	2.2	2.2	2.2	2.2	2.2	2.2	2.3
100000	2.1	2.0	2.0	2.0	2.0	1.9	1.9	1.9	1.9	1.9	1.9	1.9	1.9	1.9	2.0
neutron RBE (DSB sites)															
	shell ♯ [mean depth (cm)]														
E_n **(MeV)**	**1[0.5]**	**2[1.5]**	**3[2.5]**	**4[3.5]**	**5[4.5]**	**6[5.5]**	**7[6.5]**	**8[7.5]**	**9[8.5]**	**10[9.5]**	**11[10.5]**	**12[11.5]**	**13[12.5]**	**14[13.5]**	**15[14.5]**
10^{-8}	1.4	1.2	1.2	1.2	1.2	1.1	1.1	1.1	1.1	1.1	1.1	1.1	1.1	1.1	1.1
10^{-7}	1.3	1.3	1.2	1.2	1.2	1.1	1.1	1.1	1.1	1.1	1.1	1.1	1.1	1.1	1.1
10^{-6}	1.3	1.3	1.2	1.2	1.2	1.2	1.2	1.1	1.1	1.1	1.1	1.1	1.1	1.1	1.1
0.0001	1.2	1.2	1.2	1.2	1.2	1.2	1.2	1.2	1.2	1.1	1.1	1.1	1.1	1.1	1.1
0.001	1.2	1.2	1.2	1.2	1.2	1.2	1.2	1.2	1.2	1.1	1.1	1.1	1.1	1.1	1.1
0.01	1.3	1.2	1.2	1.2	1.2	1.2	1.2	1.2	1.2	1.2	1.1	1.1	1.1	1.1	1.1
0.1	2.0	1.7	1.5	1.4	1.3	1.2	1.2	1.2	1.2	1.2	1.2	1.2	1.1	1.1	1.1
0.2	2.3	2.0	1.8	1.6	1.4	1.3	1.2	1.2	1.2	1.2	1.2	1.2	1.1	1.1	1.2
0.5	2.4	2.3	2.1	2.0	1.8	1.7	1.6	1.5	1.4	1.3	1.3	1.2	1.2	1.2	1.2
0.8	2.3	2.3	2.2	2.1	2.0	1.9	1.8	1.7	1.6	1.5	1.5	1.5	1.4	1.4	1.3
1	2.3	2.2	2.2	2.1	2.0	1.9	1.8	1.7	1.7	1.6	1.5	1.5	1.4	1.4	1.4
2.5	2.0	2.0	2.0	2.0	2.0	2.0	2.0	2.0	1.9	1.9	1.9	1.9	1.9	1.9	1.9
5	1.8	1.8	1.8	1.8	1.8	1.8	1.8	1.8	1.8	1.8	1.8	1.8	1.8	1.8	1.8
7.5	1.7	1.7	1.7	1.7	1.7	1.7	1.7	1.7	1.7	1.7	1.7	1.7	1.7	1.7	1.7
10	1.6	1.6	1.6	1.6	1.7	1.7	1.7	1.7	1.7	1.7	1.7	1.7	1.7	1.7	1.7
15	1.6	1.6	1.6	1.6	1.6	1.6	1.6	1.6	1.6	1.6	1.6	1.6	1.6	1.6	1.6
17.5	1.6	1.6	1.6	1.6	1.6	1.6	1.6	1.6	1.6	1.6	1.7	1.6	1.6	1.7	1.6
20	1.6	1.6	1.7	1.7	1.7	1.7	1.7	1.7	1.6	1.7	1.7	1.7	1.7	1.7	1.7
22.5	1.6	1.6	1.6	1.6	1.6	1.6	1.6	1.6	1.6	1.6	1.6	1.6	1.6	1.6	1.6
25	1.6	1.6	1.6	1.6	1.6	1.6	1.6	1.6	1.6	1.6	1.6	1.6	1.6	1.6	1.6
50	1.5	1.4	1.4	1.4	1.4	1.4	1.4	1.4	1.4	1.4	1.4	1.5	1.4	1.5	1.4
Continued															

neutron RBE (DSB sites)															
	shell ♯ [mean depth (cm)]														
E_n (MeV)	**1[0.5]**	**2[1.5]**	**3[2.5]**	**4[3.5]**	**5[4.5]**	**6[5.5]**	**7[6.5]**	**8[7.5]**	**9[8.5]**	**10[9.5]**	**11[10.5]**	**12[11.5]**	**13[12.5]**	**14[13.5]**	**15[14.5]**
100	1.4	1.3	1.3	1.3	1.3	1.3	1.3	1.3	1.3	1.3	1.3	1.3	1.3	1.3	1.3
500	1.3	1.3	1.3	1.2	1.2	1.2	1.2	1.2	1.2	1.2	1.2	1.2	1.2	1.2	1.2
1000	1.3	1.2	1.2	1.2	1.2	1.2	1.2	1.2	1.2	1.2	1.2	1.2	1.2	1.2	1.2
10000	1.2	1.2	1.2	1.2	1.2	1.2	1.2	1.2	1.1	1.1	1.1	1.1	1.1	1.1	1.1
100000	1.1	1.1	1.1	1.1	1.1	1.1	1.1	1.1	1.1	1.1	1.1	1.1	1.1	1.1	1.1

Table 1. Model results for the neutron RBE for DSB cluster (upper Table) and DSB site (lower Table) induction for all tested neutron incident energies (E_n) and shells in the phantom. The average depth (in radial coordinate) for each shell is also reported.

reasonably detailed binning while limiting the simulation cost, and based on other considerations critically commented in the "Discussion" section. A three-dimensional view of the phantom and inner shells is shown in Fig. 1 (panel (b)); the tissue composition is also reported in the figure caption.

We characterized with PHITS the secondary mixed charged-particle field, generated by neutron interactions inside the phantom at the cellular and sub-cellular scales (of note, tertiary electrons account for secondary photon energy deposition in the simulations). To this aim, we used the microdosimetric tally available in PHITS: analytical functions implemented in the transport code give probability densities of microdosimetric quantities, defined in micrometric sensitive sites, in any general macroscopic target volume[26]. Specifically, the dose distribution of the lineal energy has been obtained to describe the energy deposition of neutron-induced secondary species. For a single event, the lineal energy y is defined as the ratio of the deposited energy in a sensitive site (here chosen with a diameter of 1 μm, roughly corresponding to the linear dimensions of chromosome domains) to the mean chord length of the site[27,28]. The dose distribution of the lineal energy $d(y)$ represents the probability that the dose d is deposited in the sensitive site with a lineal energy between y and $y + dy$. The first moment of the $d(y)$ distribution is referred to as the dose mean lineal energy, $\overline{y_D}$: as the expectation value of the dose distribution of y, this quantity can be interpreted as the single lineal energy value at which, on average, the dose is deposited to the target.

Within this simulation setup, for each secondary charged particle species s in the neutron-induced mixed field, we calculated:

- the relative contribution to the total neutron dose D_s, disclosing the relative importance of each species in delivering dose to the target;
- the dose mean lineal energy $\overline{y_D}_s$, correlated with its effectiveness in inducing biological (DNA) damage.The values of such two quantities for different species strongly depend on the neutron incident energy and the position inside the target. When available for all species, they fully describe the neutron field: the total neutron dose is the sum of all the dose contributions D_s, and the resulting neutron dose mean lineal energy, $\overline{y_D}_n$, is given by the weighted average of $\overline{y_D}_s$ values, using as weights the relative dose contributions D_s.

Throughout this paper, all quantities extracted from PHITS simulations are expressed as a function of neutron incident energy, regardless of the change in energy with the interactions inside the phantom.

Simulation results are always obtained with a statistics of at least 10^6 neutrons per run (2000 neutrons per batch, with 500 simulation batches per neutron energy studied), in order to reduce statistical fluctuations and keep the relative error under $\sim 10\%$. Here, statistical uncertainty was considered as given by the PHITS code, i.e. by the standard deviation of batch results. Uncertainty related to model selection, cross-section database etc. was not considered.

DNA damage predictions at the cell-nucleus scale

The Monte Carlo track-structure code PARTRAC has been extensively used in previous works, producing simulation results for the induction of a variety of DNA damage endpoints by different charged particles in a wide range of initial energies[16–18]. In particular, the more recently published database of simulation results[15,18] considers a lymphocyte-like cell nucleus in its G0/G1 cell cycle phase, containing a software representation of a 6.6 Gbp genetic makeup. The database includes the yields of specific DNA damage classes due to different light ions: ^{1}H, ^{4}He, ^{7}Li, ^{9}Be, ^{11}B, ^{12}C, ^{14}N, ^{16}O and ^{20}Ne, in an energy range from 0.5 GeV/u down to stopping. DNA damage is simulated both as direct damage, from the energy deposition of radiation to the DNA molecule, and indirect damage, simulating the production and diffusion of radical species and their attack to the DNA (in particular, explicitly considering $^{\bullet}$OH radical-mediated damage). As common in radiobiological studies, the DNA damage yields are analyzed as a function of radiation quality, choosing as indicator an estimation of the average linear energy transfer in the cell-nucleus volume. More specifically, the simulation setup consists in a 10 μm-diameter spherical cell nucleus, irradiated with ions originating from a tangential circular 10 μm-diameter source plane. The orientation of the source with respect to the nucleus in the simulation coordinate frame is changed randomly in each simulation run, thus resulting in an isotropic irradiation. For each simulation run, the fluence of particles F (number of particles fired per unit surface of the source) and the dose deposited to the cell nucleus D are stored, so that the average linear energy transfer in the cell nucleus $\frac{dE}{dx}$ can be derived from the following equation:

$$D[Gy] = 1.6{\times}10^{-9} \times \frac{dE}{dx}\left[\frac{keV}{\mu m}\right] \times F\left[cm^{-2}\right] \times \frac{1}{\rho}\left[\frac{cm^3}{g}\right] \tag{1}$$

where the factor $1.6 \cdot 10^{-9}$ comes from the chosen units. The application of Eq. (1) provides an estimation of a restricted LET = $\frac{dE}{dx}$ indicator in the cell nucleus. Its validity is however limited to particles that have enough initial energy to traverse the whole volume used for the dose evaluation. If particles stop in the cell nucleus, only the portion of the nucleus traversed by such particles (a spherical cap, whose thickness is given by the particle range) is considered for the dose and LET estimate in Eq. (1). Of note, this quantity is called LET here and in previous publications, for the sake of simplicity, though its definition remains specific to this simulation setup.

In Kundrát et al.[15], DNA damage results are given as a function of this LET indicator, and analytical functions and best-fit parameters (dependent on the class of DNA damage and on the type of particle) are given. These functions allow a quick evaluation of the expected radiation-induced DNA damage in a cell nucleus, once known the average linear energy transfer of the kind of charged particle under study in the same cell nucleus volume. In this work, they are applied to derive the damage induced by charged particles produced by neutron interactions, finally obtaining neutron-induced DNA damage, as later discussed.

In particular, two specific classes of DNA damage are considered here, both based on the definition of a double-strand break (DSB), i.e. two strand breaks appearing on opposite DNA strands within a genomic length of 10 basepairs (bp). We considered: DSB clusters, defined by the presence of at least two DSBs not separated by more than 25 bp (similar to the definition of DSB++ previously proposed by Nikijoo et al.[29,30]). If two or more DSBs are present within such short genomic length, the damage site is counted as 1 DSB cluster, and, when scoring clusters, only such complex damage sites are considered; DSB sites, scoring both isolated DSBs and their clusters, counted as 1 DSB site irrespective of their internal complexity. These definitions have also been adopted in the previous works, and provide a framework to characterize the overall chromatin breakage as well as local DSB complexity. The yields of these kinds of damage are described by their dependence on the LET estimated in the cell nucleus, given by the expression[15]:

$$Yield = (p_1 + (p_2\mathrm{LET})^{p_3})/(1 + (p_4\mathrm{LET})^{p_5}), \tag{2}$$

where *Yield* is per Gy per Gbp ($\mathrm{Gy}^{-1}\mathrm{Gbp}^{-1}$), LET in keV/$\mu$m, and p_1-p_5 are best-fit parameters depending on the damage considered and on the radiation quality. Best-fit parameters for DSB clusters and sites to be used in Eq. (2) and the corresponding functions are shown and discussed in detail in Kundrát et al.[15]. Parameters for H were used in this work to estimate the yields of DNA damage induced by deuterons and tritons (only mild deviations for DNA damage induced by different H isotopes were observed in Kundrát et al.[31]), and by electrons, positrons and pions as well (with low linear energy transfer values, as those reached by high energy protons). These analytical functions were derived to be applicable in the whole energy range investigated in PARTRAC simulations, neglecting hooks in the damage damage yields appearing at very low energies in the distal Bragg peak regions. In this work they are applied to neutron-induced charged secondary products in the whole neutron energy range explored, as later discussed. The statistical uncertainty of the simulations as well as the deviations of analytical fits from the simulation results are always below a few percent[15].

Coupling neutron transport in the human-sized phantom to the cell-nucleus scale

The previously adopted strategy[11] to couple PHITS results on neutron transport (in particular, the microdosimetric characterization of the secondary charged-particle field induced by neutrons) to the results obtained with PARTRAC on charged-particle induced DNA damage relies on the assumption that the dose mean lineal energy calculated by PHITS in a 1 μm-diameter sensitive site and averaged on a macroscopic region is an appropriate indicator of the average linear energy transfer in cell nuclei, as calculated in PARTRAC simulations with Eq. (1).

This assumption has been tested with dedicated PHITS simulations, reproducing the cell nucleus and irradiation geometry implemented in PARTRAC. The results are presented as Supplementary Material to this work. We tested the assumption for protons, as the charged particle with the largest contribution to the neutron dose, and for a heavier ion, namely oxygen, as the most abundant heavy element in the tissue. For both protons and oxygen, the LET calculated with PARTRAC and $\overline{y_D}$ calculated with PHITS in the cell nucleus are compared as a function of particle initial energy in Fig. 1S. The largest differences between such two quantities are found at initial energies higher than ≈ 10 MeV/u. However, the associated DNA damage always becomes smaller with increasing energy (decreasing LET and $\overline{y_D}$ values). In Supplementary Material, Fig. 2S, these differences are translated into differences in DNA damage yields when analytical functions from Kundrát et al.[15] are queried using LET or $\overline{y_D}$ as independent variables to calculate the yields of DNA damage. Based on the results of these test simulations, the assumption holds as an approximation, and is used in further modelling steps.

Neutron DNA damage and RBE model

Using the analytical functions from Kundrát et al.[15], the DNA damage yield associated to each charged secondary species *s* in the neutron-induced mixed field can be estimated, given the dose mean lineal energy of such species in the region of interest, $\overline{y_D}_s$. The sum of all the damage yields, each weighted by the relative contribution of the secondary species to the total neutron dose D_s, corresponds to the total DNA damage associated to neutrons $Yield_n$, namely:

$$Yield_n = \sum_s D_s Yield_s(\overline{y_D}_s) \tag{3}$$

Once the neutron-induced DNA damage is calculated, the model can be developed to calculate the corresponding RBE. The RBE is defined as the ratio of the dose of a reference radiation, typically low-LET photons, to the dose of a test radiation required to produce the same effect. It is therefore dependent on the choice of the reference radiation and on the biological endpoint considered. The ab-initio neutron RBE model refers to and it is based on the induction of different classes of DNA-damage. The fact that the damage depends on the energy of the incident neutron makes it necessary to analyze the final RBE dependence on the neutron energy.

When the classes of damage under study are linear with the radiation dose, as is the case for doses up to hundreds of Gy[32–34], the RBE can be conveniently expressed as the ratio of the damage yield following neutron irradiation to the damage yield following a low-LET reference radiation, at the same dose. In this work (as also done previously in Friedland et al.[18]), we did not perform dedicated simulations with photons as the reference radiation, but we instead derived the damage yield following low-LET radiation applying the condition LET $\rightarrow 0$ to Eq. (2), which gives the parameter p_1. The assumption underling this approach is that high energy ions (protons) induce very similar DNA damage patterns and yields as the reference photon radiation does. This holds true when ^{60}Co γ-rays (or, more generally, photons in the MeV energy range) are used as reference radiation, while possible adjustments that might be necessary when using kV X-rays as a reference are critically commented in the "Discussion" section. From these considerations, it follows that the neutron RBE is fully determined by the damage yield following neutron irradiation $Yield_n$, appropriately rescaled to the damage yield of the chosen reference radiation. Therefore, the neutron RBE for a particular kind of damage, RBE_n, can be finally evaluated as:

$$RBE_n = \frac{Yield_n}{p_1} \tag{4}$$

where p_1 is the parameter entering the analytical expression for that damage class as a function of LET: 6.8 and 0.07 Gy^{-1} GBp^{-1}, respectively for DSB sites and clusters. The RBE calculation has been performed for each of the 15 isocentric shells of the phantom, thus mapping its variation as a function of the depth inside the phantom, allowing to study, in perspective, the correlation of RBE values to possible effects and risk for tissues/organs located at the corresponding depth inside the human body.

Analytical fit to RBE model results

RBE predictions obtained for the DSB cluster endpoint in the outermost scoring region of the phantom were fitted via the following expression:

$$\begin{aligned} RBE(E_n) = q_1 &+ q_2 \exp(-q_3(\ln(E_n q_4))^2) \\ &+ q_5 \exp(-q_6(\ln(E_n q_7))^2) \\ &+ q_8 \exp(-q_9(\ln(E_n q_{10}))^2) \\ &+ \frac{q_{11} \cdot q_{12}^2}{(\ln(E_n q_{13}))^2 + q_{12}^2} \\ &+ q_{14} \exp(-q_{15}(\ln(E_n \exp(q_{16})))^2) \end{aligned} \tag{5}$$

In addition to a constant q_1, this is a sum of four Gaussian peaks and a Breit-Wigner peak in logarithmic scale of neutron energy E_n; ln denotes natural logarithm. The functional form was selected to faithfully reproduce the simulation results: the main peak around 0.5 MeV, the minor sharp peak around 20 MeV, a basis underlying these two peaks, and a broad low-energy peak; plus one Breit-Wigner peak to modulate the minor sharp peak around 20 MeV. The formula does not represent a mechanistic model of neutron RBE, but merely an analytical formula capturing the results of the performed mechanistic simulations, without aiming to use parameters with clear physical or biological interpretation or to limit the number of parameters used. The parameters were fitted with MATLAB, version R2022a[35], using a non-linear fitting model (function *nlinfit*), starting from an educated guess of their values. Best fit parameter values are: q_1 = 2.0384, q_2 = 2.041, q_3 = 0.0712, q_4 = 0.0087, q_5 = 14.1637, q_6 = 0.3131, q_7 = 2.5404, q_8 = 3.1439, q_9 = 0.611, q_{10} = 0.0383, q_{11} = 4.2598, q_{12} = 0.2139, q_{13} = 0.0538, q_{14} = 3.1486, q_{15} = 0.0099 and q_{16} = 25.0623.

Results

Neutron-induced mixed field: analysis of the energy deposition

The full information on the neutron energy deposition can be summarized in two main pieces of information for each of the secondary species *s* of the mixed field produced by neutron interactions inside the human tissue. As previously discussed, these are the relative dose contribution, D_s, and the dose mean lineal energy, $\overline{y_D}_s$ (1 μm), both derived starting from PHITS calculations. Only charged species have been considered here: the secondary photon component has been included in the electron contribution, scoring the energy deposited by tertiary electrons produced by the secondary photon interactions. All quantities are always presented as a function of the incoming neutron incident energy. Such energy might correspond to the energy of neutrons at interaction only for the most external shells and/or for energies associated to a long neutron mean free path with respect to the shell dimension. As the phantom is immersed in an isotropic neutron field, it has not to be forgotten that dose to a given shell can be delivered by secondary particles produced elsewhere in the phantom, also from neutrons coming from all possible directions.

The PHITS simulations provided the total dose D_n as well as the contributions of each of the secondary species D_s. The relative dose contribution associated to each species is simply given by the ratio D_s/D_n. Panels (a)–(c) of Fig. 2 show the relative dose contribution as a function of the neutron energy for three representative positions inside the phantom: the outermost shell (shell #1, panel (a)), an intermediate one (shell #8, panel (b)) and the innermost one (shell #15, panel (c)). Considering charged species up to Z=8, the dose contributions are virtually exhaustive of the total neutron dose up to neutron energies of 100 MeV, and they still sum up to 95-96$\%$ of the total neutron dose at the highest tested neutron energy.

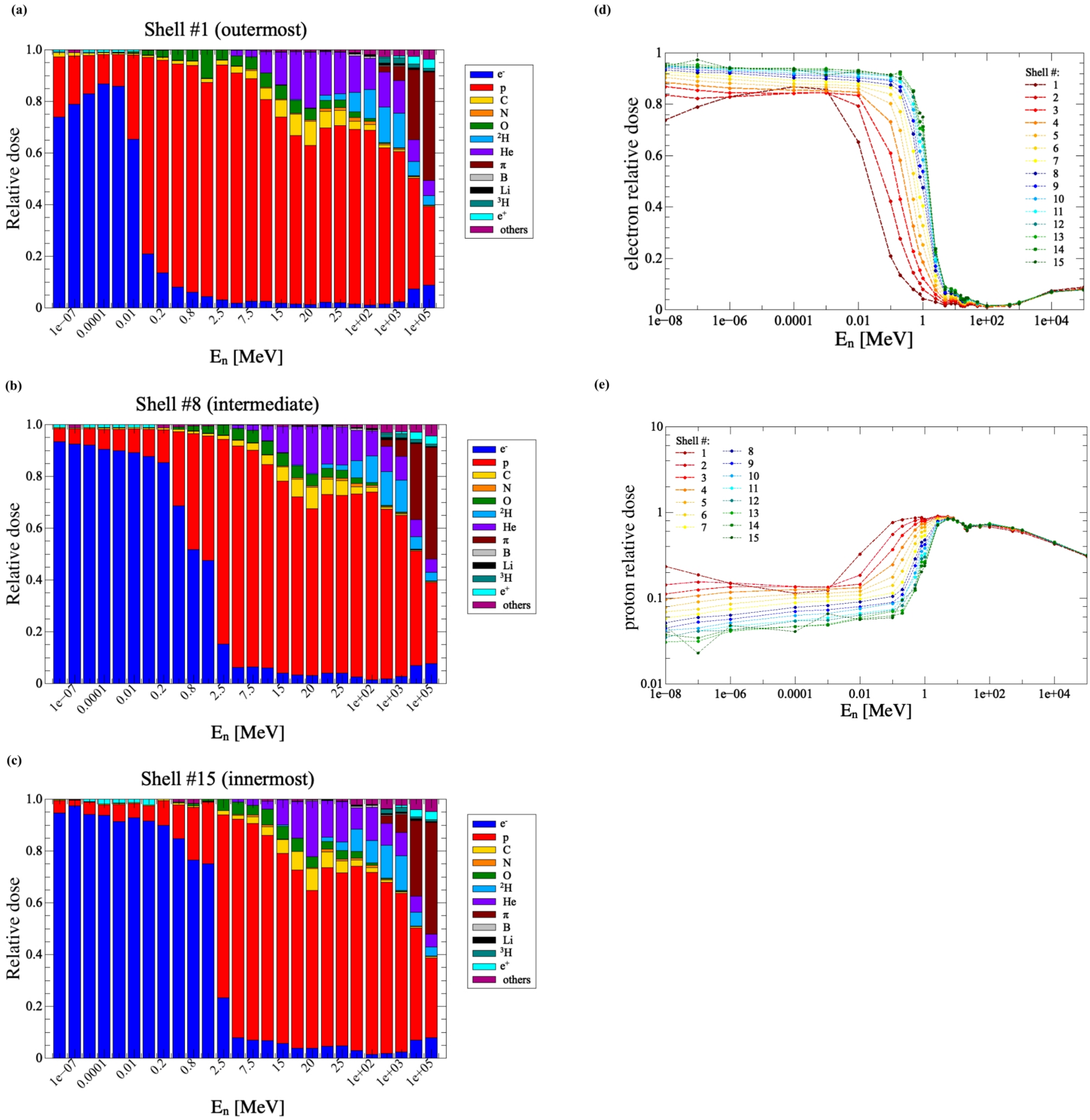

Fig. 2. Left panels: relative dose contribution of the secondary charged species in the neutron-induced mixed field, as simulated with PHITS. Results are shown as a function of the incident neutron energy E_n, for three representative shell regions of the phantom at different depths: the outermost (shell #1, (a)), the intermediate one (shell #8, (b)) and the innermost (shell #15, (c)). All neutron energy values E_n are listed explicitly in Table 1. Right panels: relative dose contributions associated to electrons (d) and protons (e) as a function of the incident neutron energy for all the 15 shell regions of the phantom. Lines are drawn to guide the eye.

The largest contribution to the neutron dose is given by secondary protons and tertiary electrons generated by interactions of secondary photons. The dominant process for low-energy neutrons in biological tissues is the neutron capture on the H nuclei, denoted as p(n,γ)d. The neutron is absorbed by a proton, with the production of a deuterium nucleus and the emission of a γ photon of 2.2 MeV, corresponding to the deuteron binding energy; subsequently, this photon undergoes further interactions, liberating and accelerating tertiary electrons. The neutron capture cross-section decreases as the neutron energy increases, which translates into a drop of the relative dose contribution of electrons. This is clearly visible in panel (d) of Fig. 2, where the relative dose contribution of electrons is shown as a function of the neutron energy E_n for all the 15 shell regions of the phantom. Moving towards the innermost shell, neutrons have the chance to be moderated upon traversing a larger tissue thickness, and thus the neutron capture probability increases for higher initial neutron energies: the E_n value, at which the electron dose contribution drop occurs, increases. The relative dose contribution associated to deuteron, the recoil product of neutron capture on proton, follows the same behaviour as the electron dose, but it is several orders of magnitude lower (not shown). After the drop, the deuteron dose contribution starts to increase again, as new reaction channels open, where d nuclei can be produced. Hence, deuteron contribution is visible in Fig. 2 (panel (a)) for neutron energies above 20 MeV only. A similar increase happens for electrons, but to a lesser extent (see Fig. 2). The proton dose component for low-energy neutrons originates from neutron capture on ^{14}N, $^{14}\mathrm{N(n,p)}^{14}$C, with the acceleration of a ^{14}C and a proton, sharing 626 keV of energy gained in the process. Such process has itself a larger cross section than p(n,γ)d capture reactions, but a lower importance due the relatively low N percentage in the tissue. For both no-threshold neutron capture processes on N and on protons, the cross-sections decrease with increasing neutron energy. These are the two dominant processes for low-energy neutrons, responsible for nearly 100$\%$ of dose deposited below 10^{-1} MeV. Interestingly, for neutron energies up to $\approx 10^{-5}$ MeV, neutron capture on ^{14}N and the associated proton component of the neutron dose show an increasing trend for the outermost shell but decreases in other shells. α particles are seen depositing dose only above a given threshold for their production, $\approx$ 5 MeV.

For high neutron energies, neutron scattering becomes the dominant process and the neutron can transfer, in a single collision, a significant amount of energy to target nuclei in the tissue. Due to the kinetics of the process, the most “efficient” collision happens with H nuclei, where the neutron can transfer all its energy to the target[1]. The energy of the accelerated proton will therefore increase with the neutron energy. Panel (e) of Fig. 2 shows how the proton contribution starts dominating the neutron dose at around $\mathrm{E}_n \approx 1$ MeV. The importance of heavier elements in depositing dose increases with increasing neutron energy and depends on several factors such as the relative abundance of the given element in human tissues, its inelastic scattering cross-section with neutrons and the reaction threshold.

For the highest tested neutron energies, reactions such as electromagnetic showers are possible, and the relative dose contribution of pions is one of the most relevant.

The second quantity extracted from the PHITS simulations is the dose distribution of the lineal energy, $d(y)$, for secondary species up to Z=8, in dependence on neutron initial energy. Ions with Z>8 were neglected, due to their above-discussed small contribution to the neutron dose. As previously discussed, the expectation value of $d(y)$ is the dose mean lineal energy $\overline{y_D}$, which can be seen as the average lineal energy at which most of the dose is deposited. The dose mean lineal energy values of all the species considered as a function of the neutron energy are shown in Fig. 3 for the same three representative shells in the phantom.

The $\overline{y_D}$ associated to electrons has a low and almost constant value, virtually independent of the neutron energy and thus of the position in the phantom. Deuteron contribution is constant as well for low E_n, as long as deuterons are the recoil products of neutron capture on protons, and then it varies as E_n increases and d is produced via different mechanisms. For E_n lower than roughly 1 MeV, the proton dose mean lineal energy value is virtually constant and quite high ($\sim$60 keV/μm, though higher local values, considering smaller microdosimetric sensitive sites, should be possible), as protons are recoiled with low energies, and then it decreases as the neutron energy increases (hence, when protons are accelerated at higher energies). α particles can be observed also in Fig. 3 only over their production threshold, and their $\overline{y_D}$ contribution decreases with the increasing neutron energy, when the alpha particles are accelerated to higher energies, thus reducing their stopping power. For heavier species, when they have a low contribution to the total neutron dose (e.g. in the highest energy neutron range), some fluctuations can be observed also in the dose mean lineal energy values, due to the poor statistics of associated neutron-induced events.

The neutron dose mean lineal energy, $\overline{y_D}_n$, is obtained as the average value of the $\overline{y_D}$ associated to secondary species, each one weighted by its relative dose contribution. Figure 4 shows $\overline{y_D}_n$ as a function of the incident neutron energy for the three representative depths in the phantom. A double-peak structure can be observed for the outermost region of the phantom (in red). The first peak, around $\mathrm{E}_n \sim$1 MeV, is due to the high value of the proton dose mean lineal energy combined with the maximum of the proton relative dose. Such a peak, in more internal regions of the phantom, becomes lower and shifted toward higher incident neutron energies, resulting therefore in not being clearly discernible. The second peak, around $\mathrm{E}_n \sim 20$ MeV and visible in all the regions of the phantom, is due to the rapid increase in the dose mean lineal energy of heavier elements (C, N and O), coupled to a maximum of their relative dose contribution. It is worth noting that, in the neutron energy region of the second peak, $\overline{y_D}_n$ reaches values higher than 100 keV/μm, which is possible only for low-energy Z>2 ions. It means that the dose mean lineal energy contribution of slow recoiling nuclei or nuclei produced via nuclear reactions plays a key role in determining the overall neutron dose mean lineal energy in the high neutron energy range. In the outermost shell, $\overline{y_D}_n$ shows an increasing trend for neutron energies decreasing from 10^{-5} MeV down to the thermal neutron region: this is due to the increase in the proton relative dose contribution with respect to the secondary photon one, and to their associated higher $\overline{y_D}$.

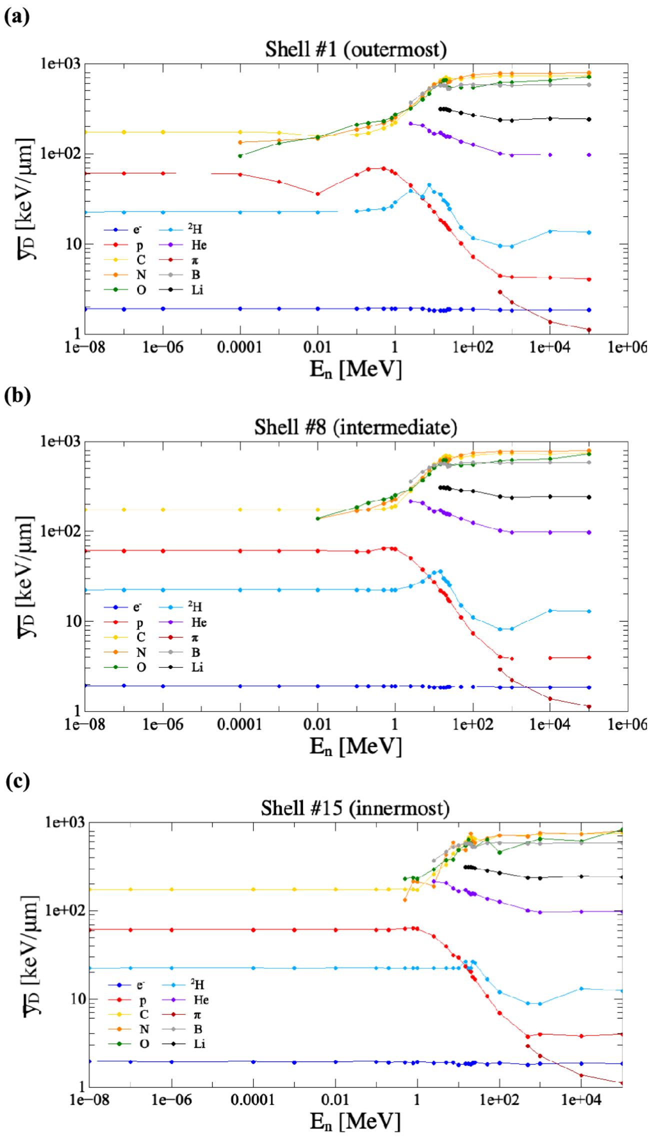

Fig. 3. Dose mean lineal energy of the secondary charged particle species composing the neutron-induced mixed field included, results from PHITS simulation. The $\overline{y_D}$ contributions are shown as a function of the incident neutron energy E_n, for three representative shell regions of the phantom: the outermost (shell #1, panel (**a**)), the intermediate one (shell #8, panel (**b**)) and the innermost (shell #15, panel (**c**)). Lines are drawn to guide the eye.

Prediction of the neutron-induced DNA damage

The yields of DSB clusters and DSB sites have been calculated with Eq. (2) for each secondary species *s*. The dose mean lineal energies $\overline{y_D}_s$ values, calculated with PHITS, were assumed representative of the restricted LET at the cell nucleus scale calculated with PARTRAC (see "Methods" and Supplementary Materials, Figs. 1S and 2S), and used in Eq. (2) with appropriate ion-dependent p_1-p_5 parameters.

The initial DNA damage yields as a function of neutron energy are presented in Fig. 5 (right vertical axis scale) for the three representative depths in the phantom. In the energy region considered for the present work, $10^{-8} - 10^5$ MeV, damage yields for the two DNA damage classes vary in the intervals: 0.1-1.1 DSB clusters $\mathrm{Gy}^{-1}\mathrm{Gbp}^{-1}$ and 6.9–16.1 DSB sites $\mathrm{Gy}^{-1}\mathrm{Gbp}^{-1}$. For both cases, the maximum value of the damage yield is associated to an initial neutron energy of 0.5 MeV when considering the outermost shell region of the phantom, where such value of the incident neutron energy is expected to correspond roughly to the actual energy at interaction. In this region, as in the most external ones, neutrons in the energy range 0.1–20 MeV are the most effective in inducing DNA damage. For the internal regions of the phantom, such maximal effectiveness is reduced, both in absolute values of damage yields, and in the neutron energy range. Of note, when moving from the $\overline{y_D}_n$ vs. neutron energy representation to the evaluation of damage, the relative height of the two peaks at 0.5 MeV and 20 MeV changes: this is due to the shape of the functions given by Eq. (2), reproducing DNA damage yields vs. LET. These functions, particularly for ions heavier than He, have a marked non monotonic behaviour, with a decrease in damage yields after reaching a maximum at ≈ 500 keV/μm and 200 keV/μm for DSB clusters

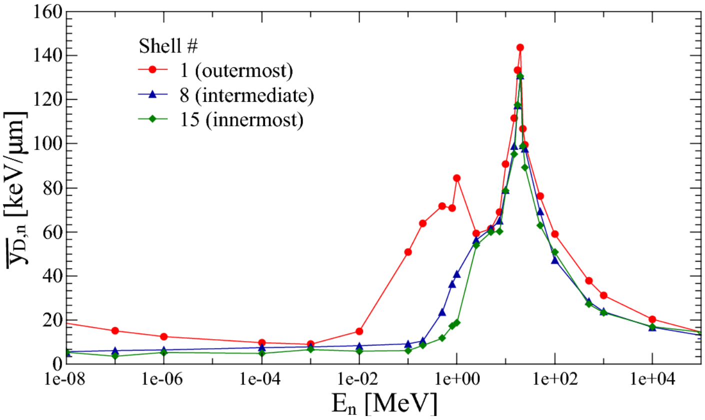

Fig. 4. Neutron dose mean lineal energy, $\overline{y_D}_n$, as a function of the incident neutron energy in three representative shell regions of the phantom: the outermost (shell #1, in red), a intermediate one (shell #8, in blue) and the innermost (shell #15, in green). Lines are drawn to guide the eye.

and sites, respectively. This behaviour, generally referred to as "overkill effect" in the literature, lowers the weights of high lineal energy components in the secondary radiation field in the overall neutron-induced damage. This effect is more relevant at neutron energies where high lineal energy components play a major role in determining the overall neutron biological effectiveness, i.e. at around 20 MeV.

Evaluation of neutron RBE for DSB cluster and DSB site induction

The neutron RBE for the induction of DSB clusters and DSB sites was calculated with Eq. (4). RBE values are shown as a function of neutron initial energy in Fig. 5 (left vertical axis scale), for the three chosen shells as representative of different depths in the phantom. Since RBE values are obtained by scaling the damage yields by a constant factor (p_1 in Eq. 4), considerations analogous to those discussed in the previous paragraph hold. Specifically, the double-peak structure characteristic of the $\overline{y_D}_n$ energy dependence translates into a double-peak RBE function: this is clearly evident for DSB clusters, and much less for DSB sites, for which the first peak heavily dominates. In terms of absolute values, the higher complexity of DSB clusters with respect to DSB sites corresponds to a lower absolute number of clusters. However, this translates into a much higher neutron RBE values, due to the much lower capability of the low-LET reference radiation to induce complex damage at the same dose (p_1 values for DSB clusters and sites are 0.07 $\text{Gy}^{-1}\text{Gbp}^{-1}$ and 6.8 $\text{Gy}^{-1}\text{Gbp}^{-1}$ respectively[15]). In the outermost shell, neutron RBE increases with neutron energy decreasing from 1 keV towards 10 meV, i.e. when approaching the thermal energy region, for both damage classes.

Figure 6 offers a visual representation of our RBE results for a better interpretation of how the biological effectiveness of a fixed initial neutron energy varies, when moving from the outer surface of the phantom to its center: as previously commented, in the most external regions the initial neutron energy might correspond to the actual energy at interaction, while at increasing depths, towards the center of the phantom, this is not the case, as incoming neutrons are slowed down. Considering the DSB cluster induction, particularly eye-catching is the mapping of the RBE of E_n= 1 MeV neutrons, which explores a wide range of values inside the phantom: the biological effectiveness of 1 MeV neutrons in inducing clusters of double-strand breaks has its highest possible values in the external regions and then significantly decreases, reaching 1/3 of its initial value in the most shielded area. The same happens for neutrons of 0.1 MeV, but covering a narrower range of RBE values. On the contrary, neutrons with the energy of 20 MeV are rather effective throughout the phantom, with limited variations with the penetration depth. Table 1 reports the complete set of RBE results obtained in this work, both for DSB clusters and DSB sites, for all tested neutron incident energies and shells in the phantom. An average depth for each shell is also reported, allowing to quickly query the Table to obtain an estimate of neutron RBE when one is interested in biological effects to shallower or deeper-seated organs in a human subject (see Supplementary Material, Table 1S, for organ-depth correlations, later commented in the "Discussion" section).

A comparison between the neutron RBE for DSB clusters in the outermost scoring region of the phantom (hence, of the maximal neutron RBE) and the current standards for radiation weighting factors, displayed in Fig. 7, shows a good qualitative agreement.

In Fig. 7, panel (b), we finally show the analytical function given by Eq. (5), fitting the same maximal RBE model results as a function of neutron energy.

Discussion

We have proposed a computational model to determine the neutron relative biological effectiveness (RBE) in inducing particular classes of DNA damage as a function of neutron incident energy and of depth inside a human-sized tissue phantom. The approach is fully ab initio, starting from neutron physical interactions in the biological tissue. It is based on the coupling of Monte Carlo radiation transport simulations, for the exposure of an ICRU44 tissue spherical phantom to monoenergetic isotropic neutrons, and of analytical functions of linear energy transfer in the cell nucleus reproducing the charged-particle induced DNA damage yield, based on

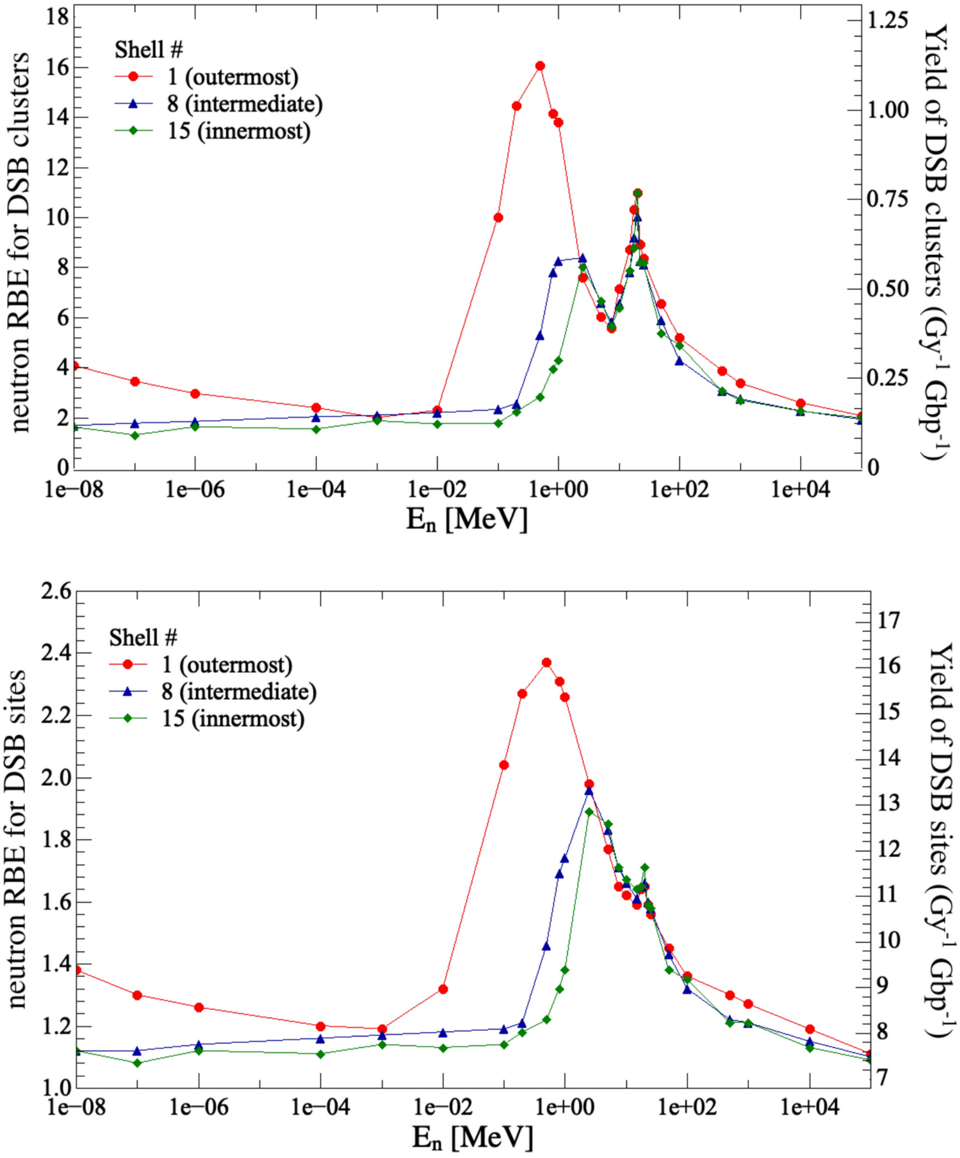

Fig. 5. Model results for the neutron RBE (left vertical scale) and damage yield Y (right vertical scale) for the induction of DSB clusters (panel (**a**)) and DSB sites (panel (**b**)), as a function of the incident neutron energy for three representative shell regions of the phantom: the outermost (shell #1, in red), a intermediate one (shell #8, in blue) and the innermost (shell #15, in green).

radiation track-structure simulation results. The strategy adopted is analogous to the one proposed in Baiocco et al.[11] with the following new developments: the test of a wider neutron energy range, down to the thermal region and up to 100 GeV (10^{-8}–10^{5} MeV); the use of new refined analytical functions for the DNA damage estimate, including the class of DSB sites; the definition of a different geometry of the phantom scoring regions, allowing for a finer and full mapping of the RBE as a function of depth.

The Monte Carlo transport code PHITS has been used to characterize the radiation mixed field generated by the neutron interactions inside the phantom. To take into account depth in the phantom in an isotropic irradiation geometry, the phantom has been built in concentric spherical shell regions. The choice of 1 cm-thick regions is based on the following considerations: thinner layers would have led to the need of a higher number of neutron transport simulation runs and to a much higher computational time, due to the fewer interactions. If the layer thickness is set to 1 cm instead, an acceptable statistical uncertainty on simulation results can be maintained; also, ideally, layers shall be selected so that they may be associated with the average depth of organs of interest in the human trunk, and most organs have linear dimensions in the cm to a few cm's range. In the Supplementary Material, we report two sets of results to justify this simplified simulation geometry. First, we performed a test simulation with a phantom divided into 30 isocentric shells (each 0.5 cm thick), whose results are fully compatible to an interpolation of results obtained with the standard 15 shells. A lower resolution binning was also tested, with the phantom divided into 10 shells only (each 1.5 cm thick), also giving compatible results with the chosen 1 cm binning. Results are shown in Fig. 3S. Moreover, we calculated the average depth

(a) Neutron RBE for DSB clusters

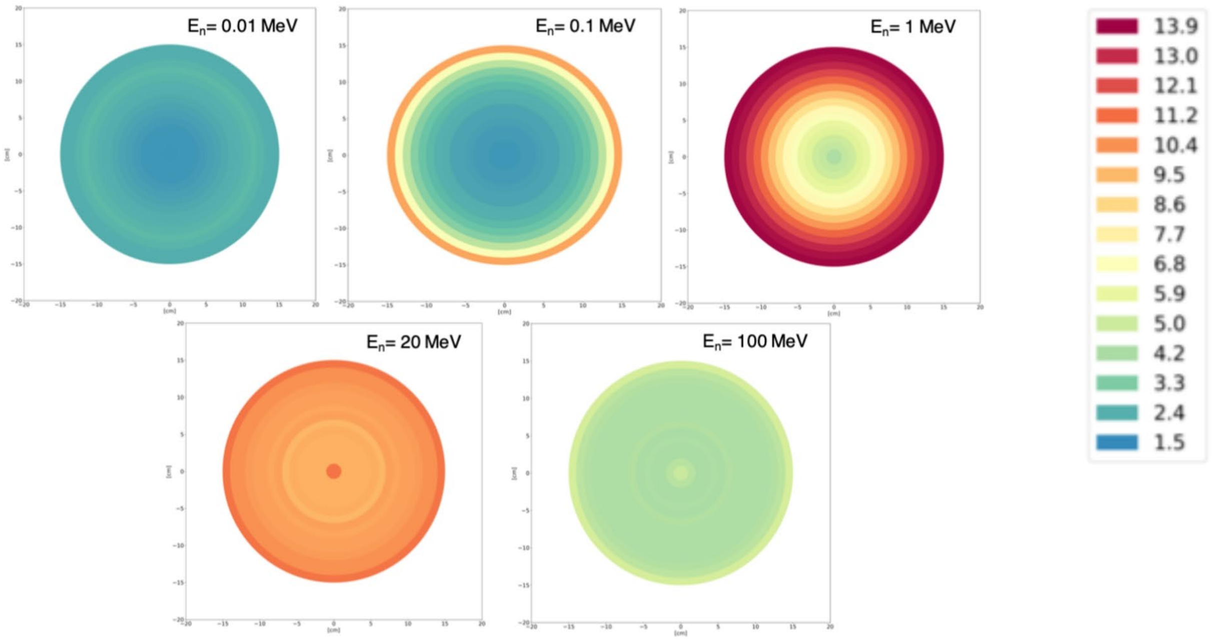

(b) Neutron RBE for DSB sites

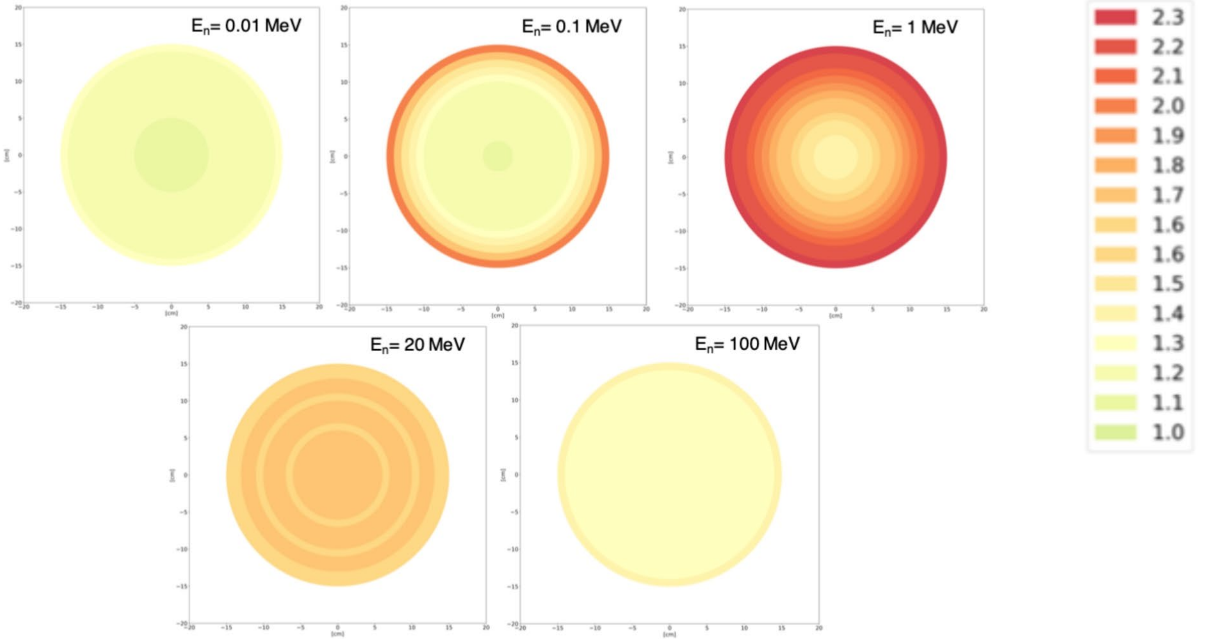

Fig. 6. Visual representation of the RBE (in color scale) for the induction of DSB clusters (panel (**a**)) and DSB sites (panel (**b**)) as a function of the depth in the phantom, i.e. in all the 15 shell regions, for chosen fixed values of the initial neutron energy E_n.

of different organs using the Geant4[36,37] mathematical phantoms (male and female). These depth values (from the phantom surface) are obtained when organs in the trunk of the phantom (ideally corresponding to the ICRU sphere) are reached by externally impinging particles in an isotropic irradiation geometry. As such, they can be associated to different phantom shells. The realistic human phantom is shown in Fig. 4S, and average depth values are reported in Table 1S. As an example, the heart is found at an average depth of ≈ 15 cm for both the female and the male mathematical phantoms used in the simulations: this suggests the use of the RBE for the innermost shell of the spherical phantom when one is interested in the biological effect of neutron exposure to the heart of a subject. Of note, due to the isotropic irradiation scenario, shallow organs can be reached by

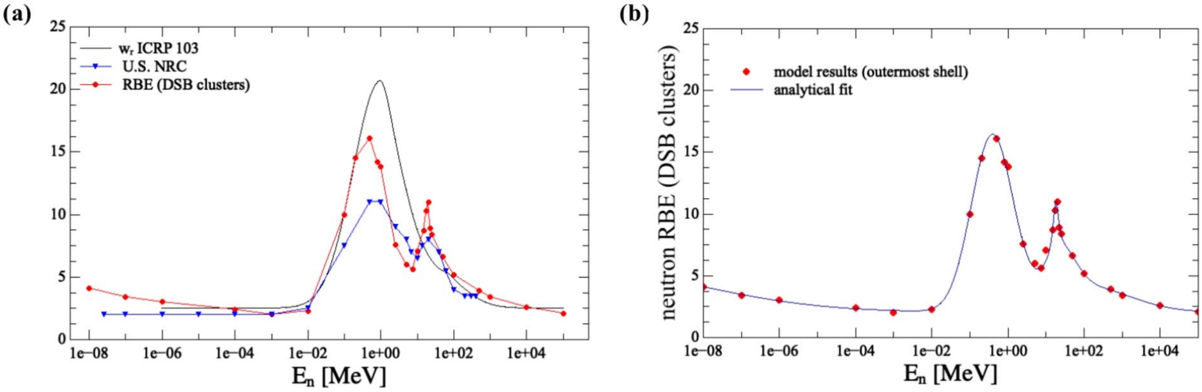

Fig. 7. Panel (**a**): qualitative comparison between the neutron RBE for DSB cluster induction, as calculated in this work in the outermost region of the phantom (in red), and the two current standard for radiation weighting factors: ICRP (analytical function in black) and U.S. NRC (dots connected by a line). For the RBE values and U.S. NRC quality factors, lines are drawn to guide the eye. Panel (**b**): analytical fit (see Eq. 5) of RBE results for the DSB cluster endpoint in the outermost region of the phantom (maximal RBE model, red dots).

particles coming from all sides of the phantom, which results in a large average depth with respect to what can be expected (e.g. ≈ 8 cm for testicles and ≈ 11 cm for breast, in the male and female phantom respectively). Full information on depth values for other organs of interests and on the procedure to obtain such results are given in the Supplementary Material. Other approaches for the development and application of the new RBE model to human phantoms with a realistic geometry and elemental composition are currently being developed.

For the purpose of the model, an exhaustive description of energy deposition in each spherical shell is provided by only two quantities for each of the secondary species composing the mixed field: the relative contribution to the total deposited dose and their dose mean lineal energy. This latter quantity, as calculated by PHITS in the phantom scoring regions using a 1 μm-diameter sensitive site, is chosen as an indicator of the average linear energy transfer in cell nuclei calculated with PARTRAC. This assumption is discussed in the Supplementary Material, with the inclusion of a set of dedicated simulations to verify the approximation (Fig. 1S and Fig. 2S). Such proposed coupling scheme between neutron-transport and charged-particle track structure simulations is presented as a first-step approximation, which heavily simplifies the simulations compared to a more detailed approach, e.g. generating energy distributions of each charged particle species produced/accelerated by neutrons with PHITS, and starting them in PARTRAC track-structure simulations. Alternative approaches of this kind are currently being developed for further comparison to the results presented in this work.

Resorting to microdosimetry we also facilitate the comparison of our RBE results to predictions of other models: of note, different radiobiological models use microdosimetric quantities to characterize radiation quality[38]. These are often calculated in a 1 μm-diameter sensitive site, as this length scale is roughly corresponding to the linear dimension of chromosome domains. Dose mean values of microdosimetric quantities are often chosen, as they are strongly correlated to the biological outcome: e.g. the dose mean lineal energy represents the lineal energy value at which, on average, the dose is deposited. The indicator of the average linear energy transfer in cell nuclei calculated with PARTRAC, called LET here and in previous works for the sake of simplicity, is less of a macroscopic quantity and bears similarity with a fluence-mean lineal energy in the 10 μm sphere representing the cell nucleus, thus also making microdosimetry as the ideal framework for the development of this RBE model.

The predictions of the DNA damage pattern as a function of neutron energy have been obtained, for all the secondary charged species, through analytical functions of the LET reproducing the results of PARTRAC track-structure simulations of the initial DNA damage induction for ions from H to Ne in a wide energy range. In particular, two classes of damage have been considered for this work: clusters and sites of double-strand breaks. The LET dependence of DSB site yields correlates well with that of cell survival, and the importance of complexity in DNA damage is well-recognized by the radiation biology community[19–21]. For all charged species reaching high linear energy transfer (or, equivalently, lineal energy) values in the cell nucleus, the trend of DNA damage gradually increases with increasing LET up to a maximum, then decreases with further increasing LET (so-called "overkill effect"). Of note, this avoids the need of a phenomenological saturation correction to high y values, often applied in other radiobiological models based on microdosimetry[39]. The damage yield associated to neutrons is given by the sum of the yields of each secondary species, weighted by its relative contribution to the neutron dose.

The linearity of the damage with the radiation dose[32–34] allows to express the RBE as the ratio between the damage yields of the test radiation and of the reference one at equal dose[11]. Instead of performing simulations with a chosen low-LET reference radiation, in this work we used damage induction in the LET → 0 limit as predicted by the same analytical functions. This is based on the assumption that, in view of all other uncertainties, differences in damage patterns and yields by very high energy ions (protons) and reference photons can be neglected. As it is known that the LET/dose mean lineal energy for photons also varies (in the few keV/μm range) with their energy, leading to possible differences in the biological effectiveness, this procedure to estimate the RBE gives results that should be compared to other works and/or benchmarked by experimental radiobiological data obtained using as a reference radiation ^{60}Co (or, more generally, photons in the MeV energy range). Instead, should a different reference radiation as 220 or 250 kVp X-ray spectra be considered, smaller RBE values can be expected, at least from a theoretical point of view: previously performed PARTRAC simulations of DNA damage following irradiations with photons as a function of their energy[40] indicate indeed an increase of the order of 10% in the DNA damage induced by 250 kV photons vs. ^{60}Co γ-rays. However, great care is needed, as experimental uncertainties in radiobiological data could easily mask such difference[41]. In light of these considerations, the choice of using the low-LET limit for charged particles as a reference radiation provides a solid and more general evaluation of the maximal RBE, also in view of radiation protection applications. Of note, an experimental benchmark of this procedure to calculate RBE for charged-particle induced DNA fragmentation has been already proposed, and the results are given as a Supplementary Information to Friedland et al., 2017[18].

Although initial DNA damage does not comprehensively represent late cellular endpoints, it is a valid indicator of radiation clustering properties and radiation quality. In particular, a complex DNA damage class such as DSB clusters likely translates into a high probability of misrepair and carcinogenesis, which underpins the biological effectiveness. Based on these consideration, the predicted neutron RBE can be discussed together with the current ICRP and U.S. NRC standards for neutron weighting factors (see Fig. 7), agreed upon by regulatory commissions on the basis of pooled RBE experimental studies, and intended to set protection values for stochastic effects of low-dose radiation. As RBE values obtained for DSB clusters have higher values with respect to those for the induction of DSB sites, and radiation protection standards are set with a conservative approach using maximal RBE values, the RBE for DSB clusters is chosen for such qualitative comparison. Also, we have considered the outermost shell of the phantom, where the initial (incident) and the actual (at interaction) neutron energy values are more likely to correspond. The rise-and-fall trend of our RBE results as a function of neutron energy confirms the energy dependence established for weighting factors, as well as the height of the first peak (at around 0.5–1 MeV neutron energy), whose value is in-between the two standards. The second RBE peak, at around 20 MeV neutron energy, is present also in U.S. NRC quality factors, but not evident in ICRP weighting factors, possibly indicating how the choice of datasets to establish radiation protection standards can significantly influence the outcome of the evaluation.

The large variation of our RBE model results with depth in the phantom, particularly for neutron energies in the range 0.1–2 MeV, also suggests that the establishment of weighting or quality factors as a function of incident neutron energy only might not be optimal, because it might lead to an overly conservative approach. This is made even more evident in Fig. 6, where RBE variations for selected given incident neutron energies are mapped in color scale throughout the phantom. Following ICRP prescriptions, considering e.g. 1 MeV incident neutrons, one should apply $\mathrm{w}_R \approx 20$ to weigh the physical absorbed dose throughout the human body, while only external tissues (e.g. the skin) would be subject to neutrons bearing such a high effectiveness in inducing biological damage. A much lower radiation weighting factor should be applied to calculate the equivalent dose to deeper-seated and more critical organs, as e.g. the bone marrow. This is indeed reflected in ICRP 123[42]: LET-dependent neutron quality factors are given as a function of initial neutron energy for different organs, together with dose-to-fluence conversion factors, for the isotropic exposure of a human reference phantom. These quality factors are indeed different for different organs for the same initial neutron energy, implicitly including depth effects in the target (in addition to organ-specific radiosensitivity) for risk assessment. A full implementation of geometry-dependent weighting factors for radiation protection purposes is certainly less practical than the existing scheme, but a strategy based on look-up tables, as those proposed in this work (Table 1), might avoid overly conservative approaches and represent a good compromise. Within the same strategy, average depths could be associated to different organs of interest, as tentatively done in Supplementary Material, Table 1S. Procedures of this kind for shell-organ association are currently being developed, including comparison of our results to neutron fluence-to-dose conversion factors and quality factors (both according to ICRP and NASA standards) available in ICRP 123[42] and derived from simulations with a realistic voxel human phantom.

It is important to recall that, from an experimental point of view, addressing the issue of neutron RBE energy dependence is very challenging: this is related to difficulties in implementing irradiation setups with monoenergetic neutron beams, and on the few energies available where this is practically feasible. On the other hand, basically no real scenario of exposure to monoenergetic neutrons exists. All these aspects make this modelling approach suitable for predictions of DNA damage and RBE in several cases: in any experimental setup for neutron radiobiology studies with quasi-monoenergetic beams, and also in any more complex neutron exposure scenario when used in combination with a definite neutron flux spectrum.

Also, neutron radiobiology studies are performed in vitro, with cell cultures, or in vivo, with animal (generally mice) exposures. The approach behind our RBE model explicitly considers the specific geometry of the target and the change in the neutron-induced charged particle field, both with target size and with penetration in a large-sized target. Of interest, other models[43,44] indicate an increase of quality factors below 10^{-3} MeV, and in-vitro experimental studies[45] have reported high RBE for DNA damage (dicentric chromosome assay and cytokinesis-block micronucleus assay) for thermal neutrons. It has to be recalled however that such increase is particularly manifested only considering a small target size, as thermal neutron dose to a large-sized receptor is always largely dominated by the photon component, hence leading to an overall low effectiveness in inducing damage. The rise of RBE for DNA damage for energies below 10^{-3} MeV is reproduced by our approach when considering the phantom most external shell. As previously commented, this is due to the proton component of the neutron dose originating from neutron capture reactions on ^{14}N. These protons, with a range in tissue of the order of 10 μm, deposit all their energy in a close vicinity of their production. On the other hand, photons from capture reactions on H have an energy of 2.2 MeV and thus can deliver dose to a given tissue also when produced far from it. For the same reason, the neutron RBE for DNA DSB cluster induction increases from ≈ 4

to ≈ 12 when a 1 mm-thick spherical tissue shell is exposed to thermal neutrons instead of the whole phantom, as shown by the results of a dedicated simulation included as Supplementary Material, see Fig. 5S. This result adds to the solidity of the proposed RBE modelling approach, again calling for a careful consideration of the target size: experimental studies reporting an increase in thermal neutron biological effectiveness with in-vitro models (small-sized receptor) shall not necessarily lead to a revision of ICRP or U.S.NRC weighting factors, as these are intended for radiation protection of a human subject (large-sized receptor).

Besides look-up tables reporting the full set of neutron RBE results obtained in this work as a function of incident neutron energy and depth in the phantom, we also provide an analytical function accurately reproducing the maximal RBE vs. energy for DSB cluster induction in the outermost shell of the phantom. This will facilitate the use of our results, and practical implementations of the maximal RBE model in relevant scenarios. As an example, in the field of medical radiation exposures, the understanding of mechanisms underlying the effectiveness of neutrons generated during particle therapy, in particular high-energy proton therapy, remains of fundamental importance. The knowledge of the neutron RBE and physical absorbed doses at any location in the patient provides relevant information to reassess the safety of possible radiotherapy alternatives and to quantify the risk of second primary cancer[46,47]. Also, our RBE model can be applied in case of exposure to the space radiation environment during human space exploration: neutrons are not present as primary radiation in space, but they are abundantly produced during interactions of primary radiation with e.g. space vehicle walls or planetary atmosphere or soil. The knowledge of the neutron biological effectiveness is therefore a fundamental ingredient for the risk assessment for astronauts. Specifically, results from this model can be coupled to estimates or measurements of the neutron flux in a definite space radiation environment when considering the neutron component, e.g. on the surface of Mars.

Data availability

the data are available upon request to the corresponding author.

Received: 20 July 2024; Accepted: 7 January 2025

References

1. Knoll, G. F. *Radiation Detection and Measurement/Glenn F. Knoll* (Wiley, 1989).
2. Hall, E. & Giaccia, A. *Radiobiology for the Radiologist* (Wolters Kluwer Health, 2012).
3. ICRP, 1991. 1990 recommendations of the international commission on radiological protection. *Ann. ICRP* **21**, 60 (1991).
4. ICRP, 2007. The 2007 recommendations of the international commission on radiological protection. *Ann. ICRP* **37**, 103 (2007).
5. ICRP, 2003. Relative biological effectiveness (RBE), quality factor (Q), and radiation weighting factor (w_R). *Ann. ICRP* **33**, 92 (2003).
6. United States Nuclear Regulatory Commission. 10 CRF 20.1004, Units of Radiation Dose. Tech. Rep., U.S. NRC (2021).
7. Ottolenghi, A., Smyth, V. & Trott, K. Assessment of cancer risk from neutron exposure—the ANDANTE project. *Radiat. Meas.* **57**, 68–73. https://doi.org/10.1016/j.radmeas.2012.10.017 (2013).
8. Pihet, P., Menzel, H., Schmidt, R., Beauduin, M. & Wambersie, A. Biological Weighting Function for RBE Specification of Neutron Therapy Beams. Intercomparison of 9 European Centres. *Radiat. Protect. Dosim.* **31**, 437–442. https://doi.org/10.1093/oxfordjournals.rpd.a080709 (1990).
9. Gerlach, R., Roos, H. & M. Kellerer, A. Heavy ion RBE and microdosimetric spectra. *Radiat. Protect. Dosim.* **99**, 413–418. https://doi.org/10.1093/oxfordjournals.rpd.a006821 (2002).
10. Stewart, R. D. et al. Rapid MCNP simulation of DNA double strand break (DSB) relative biological effectiveness (RBE) for photons, neutrons, and light ions. *Phys. Med. Biol.* **60**, 8249–8274. https://doi.org/10.1088/0031-9155/60/21/8249 (2015).
11. Baiocco, G. et al. The origin of neutron biological effectiveness as a function of energy. *Sci. Rep.* **6**, 34033. https://doi.org/10.1038/srep34033 (2016).
12. Montgomery, L., Lund, C. M., Landry, A. & Kildea, J. Towards the characterization of neutron carcinogenesis through direct action simulations of clustered DNA damage. *Phys. Med. Biol.* **66**, 205011. https://doi.org/10.1088/1361-6560/ac2998 (2021).
13. Zabihi, A. et al. Determination of fast neutron rbe using a fully mechanistic computational model. *Appl. Radiat. Isotopes* **156**, 108952. https://doi.org/10.1016/j.apradiso.2019.108952 (2020).
14. Sato, T. et al. Features of particle and heavy ion transport code system (PHITS) version 3.02. *J. Nucl. Sci. Technol.* **55**, 684–690. https://doi.org/10.1080/00223131.2017.1419890 (2018).
15. Kundrát, P. et al. Analytical formulas representing track-structure simulations on DNA damage induced by protons and light ions at radiotherapy-relevant energies. *Sci. Rep.* **10**, 15775. https://doi.org/10.1038/s41598-020-72857-z (2020).
16. Alloni, D., Campa, A., Friedland, W., Mariotti, L. & Ottolenghi, A. Track structure, radiation quality and initial radiobiological events: considerations based on the PARTRAC code experience. *IInt. J. Radiat. Biol.* **88**, 77–86. https://doi.org/10.3109/09553002.2011.627976 (2012).
17. Friedland, W., Dingfelder, M., Kundrát, P. & Jacob, P. Track structures, DNA targets and radiation effects in the biophysical Monte Carlo simulation code PARTRAC. *Mutat. Res.* **711**, 28–40. https://doi.org/10.1016/j.mrfmmm.2011.01.003 (2011).
18. Friedland, W. et al. Comprehensive track-structure based evaluation of DNA damage by light ions from radiotherapy-relevant energies down to stopping. *Sci. Rep.* **7**, 45161. https://doi.org/10.1038/srep45161 (2017).
19. Goodhead, D. T. Initial events in the cellular effects of ionizing radiations: clustered damage in DNA. *Int. J. Radiat. Biol.* **65**, 7–17 (1994).
20. Ward, J. The complexity of DNA damage: relevance to biological consequences. *Int. J. Radiat. Biol.* **66**, 427–432 (1994).
21. Georgakilas, A. G., O'Neill, P. & Stewart, R. D. Induction and repair of clustered DNA lesions: what do we know so far?. *Radiat. Res.* **180**, 100–109 (2013).
22. Hirayama, H. et al. The EGS5 code system. Tech. Rep., United States. Department of Energy (2005).
23. Iida, K., Kohama, A. & Oyamatsu, K. Formula for proton-nucleus reaction cross section at intermediate energies and its application. *J. Phys. Soc. Jpn.* **76**, 044201 (2007).
24. Ogawa, T., Sato, T., Hashimoto, S. & Niita, K. Development of a reaction ejectile sampling algorithm to recover kinematic correlations from inclusive cross-section data in Monte-Carlo particle transport simulations. *Nucl. Instrum. Meth. A* **763**, 575–590. https://doi.org/10.1016/j.nima.2014.06.088 (2014).
25. International Commission on Radiation Units & Measurements. ICRU Report 44: tissue substitutes in radiation dosimetry and measurement. *J. ICRU* **23**, 8596 (1989).

26. Sato, T., Watanabe, R., Sihver, L. & Niita, K. Applications of the microdosimetric function implemented in the macroscopic particle transport simulation code PHITS. *Int. J. Radiat. Biol.* **88**, 143–150. https://doi.org/10.3109/09553002.2011.611216 (2012).
27. International Commission on Radiation Units & Measurements. ICRU report 36: microdosimetry. *J. ICRU* **27**, 759 (1983).
28. Kellerer, A. M. *Fundamentals of Microdosimetry* (Academic Press Inc, 1985).
29. Nikjoo, H., O'Neill, P., Goodhead, D. & Terrissol, M. Computational modelling of low-energy electron-induced dna damage by early physical and chemical events. *Int. J. Radiat. Biol.* **71**, 467–483. https://doi.org/10.1080/095530097143798 (1997).
30. Nikjoo, H. & Liamsuwan, T. 9.03—biophysical basis of ionizing radiation. In *Comprehensive Biomedical Physics* (ed. Brahme, A.) 65–104 (Elsevier, 2014). https://doi.org/10.1016/B978-0-444-53632-7.00921-7.
31. Kundrát, P., Friedland, W. & Baiocco, G. Track structure-based simulations on DNA damage induced by diverse isotopes. *Int. J. Mol. Sci.* **23**, 7859. https://doi.org/10.3390/ijms232213693 (2022).
32. Kreipl, M. S., Friedland, W. & Paretzke, H. G. Interaction of ion tracks in spatial and temporal proximity. *Radiat. Environ. Biophys.* **48**, 349–359. https://doi.org/10.1007/s00411-009-0234-z (2009).
33. Barnard, S., Bouffler, S. & Rothkamm, K. The shape of the radiation dose response for dna double-strand break induction and repair. *Genome Integr.* **4**, 1. https://doi.org/10.1186/2041-9414-4-1 (2013).
34. Löbrich, M., Rydberg, B. & Cooper, P. K. Repair of x-ray-induced dna double-strand breaks in specific not i restriction fragments in human fibroblasts: joining of correct and incorrect ends. *Proc. Natl. Acad. Sci.* **92**, 12050–12054. https://doi.org/10.1073/pnas.92.26.12050 (1995).
35. The MathWorks Inc. Optimization Toolbox version: R2022a, Natick, Massachusetts. https://www.mathworks.com (2022).
36. Geant4. https://geant4.cern.ch/ (2024).
37. Agostinelli, S. et al. Geant4-a simulation toolkit. *Nucl. Instrum. Methods Phys. Res. Sect. A: Acceler. Spectrom. Detect. Assoc. Equip.* **506**, 250–303. https://doi.org/10.1016/S0168-9002(03)01368-8 (2003).
38. Bellinzona, V. E. et al. Linking microdosimetric measurements to biological effectiveness in ion beam therapy: A review of theoretical aspects of mkm and other models. *Front. Phys.* **8**, 7859. https://doi.org/10.3389/fphy.2020.578492 (2021).
39. Kase, Y. et al. Microdosimetric measurements and estimation of human cell survival for heavy-ion beams. *Radiat. Res.* **166**, 629–638. https://doi.org/10.1667/RR0536.1 (2006).
40. Friedland, W., Kundrát, P., Schmitt, E., Becker, J. & Li, W. Modeling DNA damage by photons and light ions over energy ranges used in medical applications. *Radiat. Protect. Dosimetry* **183**, 84–88. https://doi.org/10.1093/rpd/ncy245 (2018). https://academic.oup.com/rpd/article-pdf/183/1-2/84/28670297/ncy245.pdf.
41. Kocher, D. & Hoffman, F. O. Ncrp report 181, evaluation of the relative effectiveness of low-energy photons and electrons in inducing cancer in humans: a critique and alternative analysis. *Health Phys.* **116**, 817–827. https://doi.org/10.1097/HP.0000000000001011 (2019).
42. ICRP, 2013. Assessment of radiation exposure of astronauts in space. *Ann. ICRP* **42**, 123 (2013).
43. Cross, W. & Ing, H. Conversion and quality factors relating neutron fluence and dosimetric quantities. *Radiation Protection Dosimetry* **10**, 29–42. https://doi.org/10.1093/oxfordjournals.rpd.a079409 (1985).
44. Stinchcomb, T. G. & Borak, T. B. Neutron quality parameters versus energy below 4 MeV from microdosimetric calculations. *Radiat. Res.* **93**, 1–18 (1983).
45. Paterson, L. C. et al. High-accuracy relative biological effectiveness values following low-dose thermal neutron exposures support bimodal quality factor response with neutron energy. *Int. J. Mol. Sci.* **23**, 1456. https://doi.org/10.3390/ijms23020878 (2022).
46. Schneider, U., Hälg, R. A., Baiocco, G. & Lomax, T. Neutrons in proton pencil beam scanning: parameterization of energy, quality factors and RBE. *Phys. Med. Biol.* **61**, 6231–6242. https://doi.org/10.1088/0031-9155/61/16/6231 (2016).
47. Schneider, U., Hälg, R. A. & Lomax, T. Neutrons in active proton therapy: parameterization of dose and dose equivalent. *Zeitschri. Med. Phys.* **27**, 113–123. https://doi.org/10.1016/j.zemedi.2016.07.001 (2017).

Acknowledgements

The authors want to acknowledge Dr. Werner Friedland for support and interpretation of PARTRAC simulation results.

Author contributions

A.M., G.B. conceived the study; A.M., V.Q., P.K., C.C., L.B. and G.B. performed the simulations; A.M., V.Q., P.K. and G.B. analysed the results; A.M., V.Q., P.K., I.G., L.L., O.I., A.P., L.D.F., G.S.A., L.L., V.B., L.N., C.C., L.B. and G.B. interpreted the results; A.M. and G.B. wrote the manuscript; all authors edited and reviewed the manuscript.

Funding

The work was carried out thanks to institutional fundings of the University of Pavia, Italy, and NPI, Czechia. The work was also partially supported by the Italian Space Agency (Agenzia Spaziale Italiana, ASI) in the framework of the "SVILUPPO DI PROGETTI/ESPERIMENTI SCIENTIFICI NELL'AMBITO DELLO STUDIO DEGLI EFFETTI CAUSATI DALL'ESPOSIZIONE A RADIAZIONI E DALLA GRAVITÀ ALTERATA SUI SISTEMI BIOLOGICI, E DELLO SVILUPPO DI CONTROMISURE PER LA MITIGAZIONE DEL RISCHIO IN FUTURI SCENARI DI ESPLORAZIONE SPAZIALE OLTRE LEO" initiative through the contract ASI N. 2024-15-U.

Competing interests

the authors declare no competing interests.

Additional information

Supplementary Information The online version contains supplementary material available at https://doi.org/10.1038/s41598-025-85879-2.

Correspondence and requests for materials should be addressed to G.B.